

---

*Research Article: New Research | Sensory and Motor Systems*

## **Modeling physiological sources of heading bias from optic flow**

<https://doi.org/10.1523/ENEURO.0307-21.2021>

**Cite as:** eNeuro 2021; 10.1523/ENEURO.0307-21.2021

Received: 19 July 2021

Revised: 1 September 2021

Accepted: 20 September 2021

---

*This Early Release article has been peer-reviewed and accepted, but has not been through the composition and copyediting processes. The final version may differ slightly in style or formatting and will contain links to any extended data.*

**Alerts:** Sign up at [www.eneuro.org/alerts](http://www.eneuro.org/alerts) to receive customized email alerts when the fully formatted version of this article is published.

Copyright © 2021 Yumurtaci and Layton

This is an open-access article distributed under the terms of the Creative Commons Attribution 4.0 International license, which permits unrestricted use, distribution and reproduction in any medium provided that the original work is properly attributed.

Modeling physiological sources of heading bias from optic  
flow

Abbreviated title: Modeling heading bias from optic flow

Sinan Yumurtaci & Oliver W. Layton\*

Department of Computer Science, Colby College, Maine, USA

\* [oliver.layton@colby.edu](mailto:oliver.layton@colby.edu)

1  
2  
3  
4  
5  
6  
7

## Abstract

Human heading perception from optic flow is accurate for directions close to the straight-ahead and systematic biases emerge in the periphery (Sun, Zhang, Alais, & Li, 2020; Cuturi & Macneilage, 2013). In pursuit of the underlying neural mechanisms, primate brain area MSTd has been a focus because of its causal link with heading perception (Gu, Deangelis, & Angelaki, 2012). Computational models generally explain heading sensitivity in individual MSTd neurons as a feedforward integration of motion signals from area MT that resemble full-field optic flow patterns consistent with the preferred heading direction (Mineault, Khawaja, Butts, & Pack, 2012; Britten, 2008). In the present simulation study, we quantified within the structure of this feedforward model how physiological properties of MT and MSTd shape heading signals. We found that known physiological tuning characteristics generally supported the accuracy of heading estimation, but not always. A weak-to-moderate overrepresentation of peripheral headings in MSTd garnered the highest accuracy and precision out of the models that we tested. The model also performed well when noise corrupted high proportions of the optic flow vectors. Such a peripheral MSTd model performed well when units possessed a range of receptive field sizes and were strongly direction tuned. Physiological biases in MT direction tuning toward the radial direction also supported heading estimation, but the tendency for MT preferred speed and receptive field size to scale with eccentricity did not. Our findings help elucidate the extent to which different physiological tuning properties influence the accuracy and precision of neural heading signals.

## Significance Statement

31

Using vision to perceive direction of self-motion (heading) lies at the heart of our ability to effectively move through the world. Prior work has shown that monkey brain area MSTd is involved in heading perception. We simulated in a computational model how physiological tuning properties of areas MT and MSTd influence neural heading signals. We found that a neural representation of heading biased toward the periphery, in combination with other factors, best supported the accuracy and precision of heading estimates. We draw on existing models and known physiology to promote the broad applicability of our findings. Our analysis helps improve our understanding of the neural mechanisms underlying heading perception.

32  
33  
34  
35  
36  
37  
38  
39  
40

## Introduction

41

Self-motion through the world produces expansive motion patterns on the eye known as optic flow (Gibson, 1950). The optic flow radiates from a single point known as the focus of expansion (FoE) that specifies the direction of travel (heading) when the observer moves forward along a straight path through a rigid environment without sources of rotation, such as eye movements (Figure 1a-b). Under such conditions, humans are indeed capable of accurately perceiving heading from optic flow (Warren & Hannon, 1988; Van Den Berg, 1992), though errors in heading judgments do arise when the FoE is offset from the straight-ahead direction (i.e. observer moves toward the periphery; Figure 1c-d) (Warren & Kurtz, 1992; Crane, 2012; Cuturi & Macneilage, 2013). The error tends to be biased toward the center (straight-ahead direction) and ranges from several degrees for central headings to 10° at the periphery (Figure 1d;  $\alpha > 0$ ) (Llewellyn, 1971; Johnston, White, & Cumming, 1973; Cutting, Springer, Braren, & Johnson, 1992; Warren & Saunders, 1995; Royden & Hildreth, 1996; Layton & Fajen, 2016b; Sun et al., 2020).

42  
43  
44  
45  
46  
47  
48  
49  
50  
51  
52  
53  
54  
55

While the neural basis of heading perception is unknown, a casual link has been established with the dorsal medial superior temporal area (MSTd) in primate

56  
57

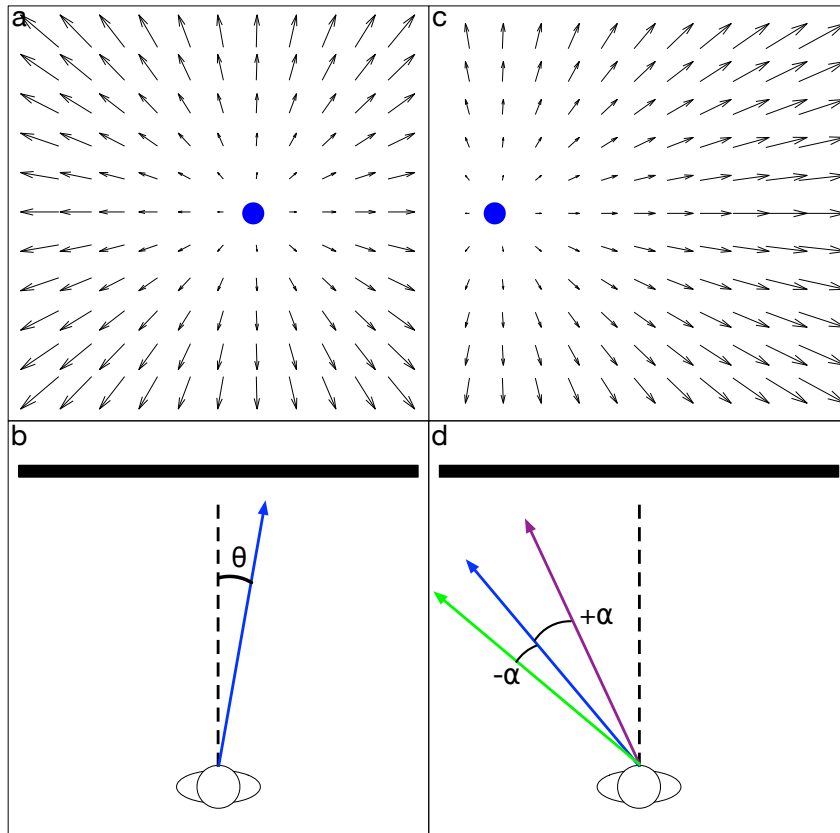


Figure 1: (a) Idealized optic flow experienced by an observer heading  $+10^\circ$  to the right of the straight-ahead direction (FoE indicated by blue disk). (b) Bird's eye view of scenario in (a). Dashed line indicates the straight-ahead direction, blue solid arrow indicates the observer's heading  $\theta$ . (c) Optic flow experienced by an observer moving at a peripheral  $-40^\circ$  heading. (d) Top-down bird's eye view of the scenario from (c), which highlights our convention for representing heading bias. Purple solid arrow illustrates underestimation of the judged heading angle or center bias (heading error  $\alpha > 0^\circ$  toward the straight-ahead direction) and green solid arrow illustrates overestimation of the judged heading angle or peripheral bias (heading error  $\alpha < 0^\circ$  away from the straight-ahead direction). The optic flow shown in top panels reflects a  $90^\circ$  field of view.

cortex (Britten & Van Wezel, 1998; Gu et al., 2012). MSTd neurons demonstrate 58  
sensitivity to full-field motion patterns that resemble those experienced during 59  
self-motion (e.g. Figure 1a,c) (Duffy & Wurtz, 1995; Gu, Watkins, Angelaki, & 60  
Deangelis, 2006). Tuning to the FoE position in the pattern along with numerous 61  
other visual and nonvisual signals that arise during self-motion has supported the view 62  
that MSTd produces neural signals that reflect heading estimation (Tanaka et al., 63  
1986; Graziano, Andersen, & Snowden, 1994; Gu et al., 2006; Duffy & Wurtz, 1991). 64  
An important predictor of MSTd activity is the medial temporal area (MT) (Mineault 65  
et al., 2012), a motion sensitive area situated earlier in the visual hierarchy (Van Essen 66  
& Maunsell, 1983) that sends feedforward signals to MSTd. Most motion-sensitive 67  
neurons in MT are tuned to direction and speed and have much smaller receptive 68  
fields than neurons in MSTd (Born & Bradley, 2005). 69

The prevailing hypothesis is that heading sensitivity emerges in MSTd through the 70  
feedforward integration of local, MT-like motion signals across the visual field in 71  
specific radial motion “templates” that are compatible with the preferred heading 72  
direction (Figure 2a). This view has been supported by computational models, which 73  
have helped elucidate possible neural mechanisms and make quantitative 74  
predictions (Perrone & Stone, 1998; Perrone, 2012; Browning, Grossberg, & Mingolla, 75  
2009; Layton, Mingolla, & Browning, 2012; Royden, 2002). Despite their focus on 76  
biological plausibility, these models tend to implicitly assume that MT and MSTd 77  
cells possess uniform sensitivity to heading, direction, speed, and other physiological 78  
properties across the visual field. This assumption, which has not been supported by 79  
neural data (Britten, 2008; Born & Bradley, 2005), may have important consequences 80  
in our understanding of the neural mechanisms underlying heading perception. 81

Our aim was to investigate how known physiological tuning properties (e.g. 82  
heading, direction, and speed; receptive field size) may interact to shape heading 83  
signals. We explored the influence of neural tuning in a template model of MT-MSTd 84  
focused on simplicity to make our findings broadly applicable. Our simulations 85  
quantify how the following physiological properties of MT and MSTd influence 86  
heading estimation: 87

- The degree to which tuning across MSTd overrepresents central or peripheral headings (Gu et al., 2006). 88  
89
- The considerable range of MSTd receptive field (RF) sizes (Tanaka et al., 1986). 90
- Bias in MT direction tuning toward a global radially expanding pattern (Albright, 1989). 91  
92
- The tendency for MT preferred speed (Maunsell & Van Essen, 1983a; Mikami, Newsome, & Wurtz, 1986) and RF size (Raiguel, Van Hulle, Xiao, Marcar, & Orban, 1995; Tanaka et al., 1986) to increase with eccentricity. 93  
94  
95

Our simulations characterize the accuracy and variability of heading estimates derived from families of MT and MSTd models that implement different physiological tuning properties. To contextualize the results, we considered both models constrained by findings from the aforementioned physiological studies and counterfactual models. For example, we simulated MSTd models all along the center-peripheral continuum, not only those with an overrepresentation of peripheral headings (Gu et al., 2006). Our second major goal was to characterize the sensitivity of each model under non-idealized conditions. To this end, we simulated each model with optic flow that contains noise in the direction and speed of the motion vectors.

## Materials and Methods 105

### Optic flow stimuli 106

Optic flow produced by a virtual observer translating through a 3D dot cloud served as the input to the neural models of MT and MSTd. We represented the environment in a standard 3D coordinate system wherein the observer's eye was centered at the origin, the positive  $Z$  axis aligned with the optical axis in front of the observer, and the  $X$  and  $Y$  axes followed right-handed conventions. The scene contained 300 dots ( $T$ ) that occupied random 3D ( $X, Y, Z$ ) positions within a 300 x 300 x 100 m volume beginning 1 m front of the observer (Table 1). Each model simulation consisted of a two second, 107  
108  
109  
110  
111  
112  
113

Parameter	Description	Value
$\vec{e}$	3D dot cloud extent	300 x 300 x 100 m
$\theta$	Observer heading	$[-50^\circ, -45^\circ, \dots, 50^\circ]$
$o$	Observer speed	1.5 m/sec
$h$	Observer height	1.61 m
$v$	Field of view	90°
$f$	Focal length	1.74 cm
$T$	Dots in scene	300
$n$	Noise dot proportion	[0.7, 0.8, 0.9]
$n_m$	Maximum random ( $X, Y, Z$ ) displacement of each noise dot around its constant observer-relative position on each frame	1 m
$F$	Duration	2 sec (60 frames)
$\vec{p}$	Spatial resolution	128 x 128 pixels

Table 1: Parameters that characterize the optic flow inputs used to simulate neural models of MT and MSTd.

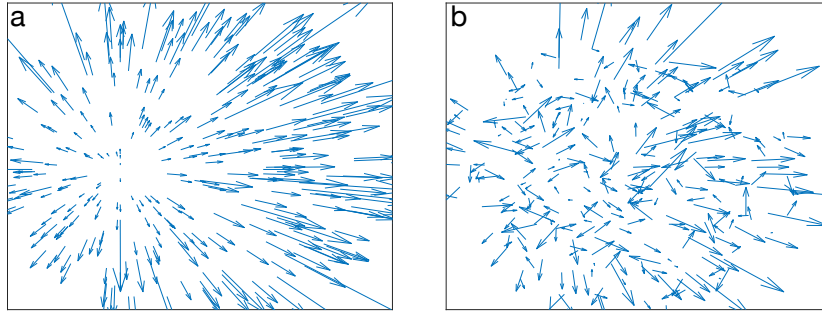


Figure 2: Sample frames from optic flow stimuli (a) Self-motion along a  $-20^\circ$  heading through a 3D dot cloud (b) Same scenario as (a) with 70% noise ( $n = 0.7$ ).

60 frame ( $F$ ) digital video of simulated self-motion at a speed of 1.5 m/sec ( $o$ ) along 114  
 one of 21 heading directions ( $\theta$ ) equally spaced along the horizontal midline (i.e.  $X$  115  
 axis): between  $-50^\circ$  and  $+50^\circ$  in steps of  $5^\circ$ . We generated the corresponding optic 116  
 flow analytically using the optic flow equations (Longuet-Higgins & Prazdny, 1980): 117

$$\begin{pmatrix} \dot{x} \\ \dot{y} \end{pmatrix} = \frac{1}{Z} \begin{pmatrix} -f & 0 & x \\ 0 & -f & y \end{pmatrix} \begin{pmatrix} T_x \\ T_y \\ T_z \end{pmatrix} \quad (1)$$

where  $\dot{x}$  and  $\dot{y}$  represent the horizontal and vertical components, respectively, of the motion vector that occupies position  $(x, y)$  on the simulated observer's retina,  $f$  is the focal length of the model eye and the vector  $\vec{T} = (T_x, T_y, T_z)'$  represents the observer's instantaneous translation through the environment. We derived the 2D retinal coordinates  $(x, y)$  by projecting the 3D dots using the standard pinhole camera model:  $(x, y) = f/Z(X, Y)$ . We scaled and discretized the positions and motion vectors  $(x, y, \dot{x}, \dot{y})$  to a 128 x 128 pixel grid ( $\vec{p}$ ). By simple trigonometry and the fact that the observer only moved along horizontal headings, the translation vector reduces to  $\vec{T} = (s \sin \theta, 0, s \cos \theta)'$ .

We maintained a constant optic flow density throughout each video by clipping and replacing motion vectors that exited the 90° field of view ( $v$ ) or came within 1 m in depth of the observer. Figure 2a shows a sample frame of optic flow corresponding to self-motion along a -20° heading. Table 1 summarizes the parameters used to generate the optic flow inputs.

### Noise conditions

We designed noise conditions that manipulated the signal-to-noise ratio in the optic flow field, emulating the approach of Van Den Berg (1992). We replaced a proportion  $n$  of the 300 dots in the 3D cloud with those that moved randomly in a reference frame that moved with the observer. These “noise dots” did not appear to approach the observer throughout each video like the rigid “non-noise dots” did. Instead, they occupied a constant mean position in the 3D dot cloud relative to the observer and drifted by a random amount between 0 and  $n_m$  m independently in  $X$ ,  $Y$ , and  $Z$  on each frame of video. As with the optic flow stimuli without noise, we maintained a constant dot density across the display by replacing dots that leave the field of view. This type of noise had the desirable effect of introducing locally discrepant directions across the optic flow field with variations in speed that both were anchored in the background statistics and did not drastically change throughout the video. Figure 2b shows a sample frame of optic flow corresponding to self-motion along a -20° heading with noise level  $n = 0.7$ . We simulated 3 noise levels: 70%, 80%, 90%. We selected

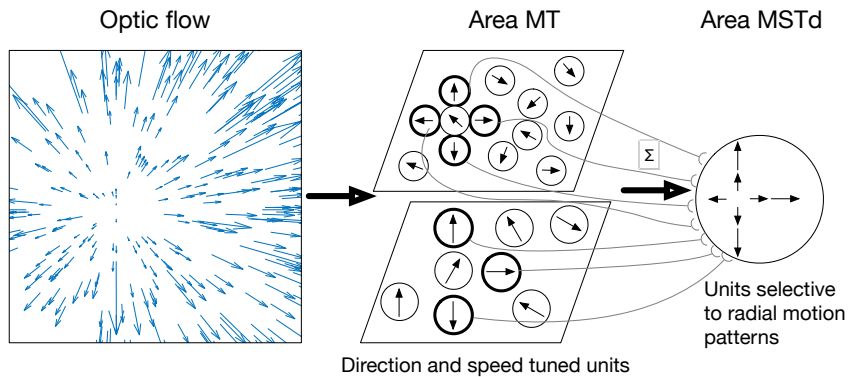


Figure 3: Schematic showing the architecture of MT-MSTd template models. Direction and speed tuned units in MT activate to the optic flow input and send feedforward signals to MSTd. Connections are structured such that tuning preferences in MT match a radial template pattern consistent with self-motion in a particular direction.

such high proportions of noise following preliminary testing that showed that most  
 model parameters were robust to more moderate amounts of noise.

### Neural model of MT and MSTd

We simulated a neural model of brain areas MT and MSTd that has the same  
 fundamental structure as existing template models (Hatsopoulos & Jr, 1991; Warren  
 & Saunders, 1995; Perrone & Stone, 1998; Perrone, 2012; Browning et al., 2009;  
 Layton et al., 2012; Royden, 2002; Raudies & Neumann, 2010). Our aim was not to  
 implement any specific model; rather we sought to create a “default” template model  
 that encapsulates computations that are fundamental to the family. In a series of  
 computational experiments, we either substituted mechanisms or varied model  
 parameters to assess the influence on heading estimates. To focus on the computations  
 within MT and MSTd, we adhered to an assumption commonly made by template  
 models that the optic flow input directly stimulates model MT units, abstracting away  
 V1 and other earlier areas (Figure 3).

We begin by presenting the “default” MT-MSTd template model structure and its  
 parameters. Subsequent sections describe which specific parametric and mechanistic

variations that were chosen to construct different families of the template model. We selected the default structure and parameter values by examining which produced the most accurate heading estimates within physiologically plausible ranges, all other factors remaining equal. Note that because this selection process considered the impact of each parameter on heading estimates one at a time, the resulting set of parameters may not correspond to the global optimum in the model's large parameter space. Table 2 summarizes the default parameters used in model MT simulations and Table 3 summarizes those in model MSTd.

#### Model area MT

Parameter	Description	Value
$N_{MT}$	Number of MT units	225
$\vec{c} = (c_x, c_y)$	Coordinates of visual field center	$(45^\circ, 45^\circ)$ / (64, 64) pixels
$\vec{r} = (r_x, r_y)$	Coordinates of MT RF center	Arranged in a 15 x 15 grid spaced apart by $7.1^\circ$ (8 pixels)
$\sigma_d$	Maximum extent of random deviation in MT direction preference about the radial direction	$180^\circ$
$\sigma_r$	Effective RF radius	$6^\circ$ (7 pixels)
$\sigma_v$	Sensitivity to optic flow that differs from the preferred direction	$10^\circ$
$\sigma_s$	Sensitivity to optic flow that differs from the preferred speed	$0.5^\circ/sec$ (0.45 pixels / sec)
$\alpha_{MT}$	MT activation passive decay rate	0.1
$\beta_{MT}$	MT activation upper bound	2.5
$dt$	Integration time step	$0.1 \text{ frame}^{-1}$ ( $0.003 \text{ sec}^{-1}$ )

Table 2: Summary of default model MT parameters used in simulations.

**MT unit placement** Model area MT consists of 225 ( $N_{MT}$ ) direction and speed tuned units that integrate optic flow within their RF (Figure 3). In experiments focusing on MSTd, we arranged the RF centers in a 15 x 15 grid spaced by  $7.1^\circ$  (measured relative to the fovea) to afford overlap among adjacent RFs. We otherwise distributed their RFs randomly across visuotopic space.

**MT direction selectivity** We parameterized MT direction selectivity around the physiological bias toward an idealized radial pattern that radiates out from the center

of the visual field ( $0^\circ$  heading) (Albright, 1989). Each MT unit's direction preference obeys

$$d^* = \arctan\left(\frac{r_y - c_y}{r_x - c_x}\right) + x_d \quad (2)$$

where  $\vec{c} = (c_x, c_y)$  indicates the center position of the visual field and  $\vec{r} = (r_x, r_y)$  indicates the position of the RF center. The variable  $x_d$  is a random variate sampled from the uniform distribution

$$x_d \sim \mathcal{U}[-\sigma_d/2, \sigma_d/2] \quad (3)$$

where  $\sigma_d$  is the two-sided maximum extent of random deviation. Taken together, 177  
 Eqs. 2-3 assign each cell a random direction preference centered on the idealized radial 178  
 direction based on the MT cell's RF position. In the default model configuration, we 179  
 set  $\sigma_d = 180^\circ$ , which means that each MT unit's direction preference is within  $90^\circ$  of 180  
 the radial direction. For example, a neuron whose RF is centered to the right side of 181  
 the visual field along the horizontal midline has direction selectivity within  $90^\circ$  of 182  
 the rightward direction—directions in between upward and downward are possible. At the 183  
 extremes  $\sigma_d = 0^\circ$  would imply that population direction selectivity would strictly 184  
 follow a radial pattern and  $\sigma_d = 360^\circ$  would imply uniform random direction 185  
 selectivity across MT. 186

**MT speed selectivity** In the default model we sampled speed preferences from a uniform distribution spanning the dynamic range of speeds present in the optic flow inputs:

$$s^* \sim \mathcal{U}[\min \vec{s}, \max \vec{s}] \quad (4)$$

where  $\vec{s}$  represents the optical speeds of the 300 input motion vectors, computed as:

$$\vec{s} = \sqrt{(\vec{x})^2 + (\vec{y})^2} \quad (5)$$

**MT unit net input** The input signal to each MT unit depends jointly on the distance of the motion from the RF center  $I_c$ , the similarity between the preferred and optic flow directions  $I_v$ , and the similarity between the preferred and optic flow speed

$I_s$ :

$$I_{MT} = \frac{1}{T} \sum_{j=1}^T I_{c,j} I_{v,j} I_{s,j} \quad (6)$$

That is, each MT cell averages over the set of distance-weighted direction and speed inputs that it receives. We assumed that each unit had a Gaussian-shaped RF: sensitivity to optic flow is greatest nearby the RF center and declines with distance, all other factors remaining equal. The distance between the 300 optic flow vectors and each MT unit's RF center is computed as:

$$\vec{I}_c = \exp\left(-\frac{\left(\left(\vec{x} - r_x\right)^2 + \left(\vec{y} - r_y\right)^2\right)}{2\sigma_r^2}\right) \quad (7)$$

where  $\sigma_r$  defines to the effective RF radius—a circle of radius  $\sigma_r$  contains  $\approx 95\%$  of the RF area. We set  $\sigma_r = 6^\circ$ , which compares favorably with data on MT RF size (Deangelis & Uka, 2003). 187  
188  
189

The direction input depends on the difference between the cell's preferred angle and those present within the RF. Equality between the preferred and optic flow angles garners the highest input and the signal decreases as the mismatch grows according to a Gaussian function:

$$\vec{\Delta}_v = \text{atan2}\left(\vec{y}, \vec{x}\right) - d^* \quad (8)$$

$$\vec{I}_v = \exp\left(-\frac{\vec{\Delta}_v^2}{2\sigma_v^2}\right) \quad (9)$$

In Eq. 9,  $\sigma_v = 10^\circ$  represents the sensitivity to optic flow directions that deviate from the preferred direction. 190  
191

Each MT unit demonstrates similar Gaussian tuning to differences between optic flow and preferred speeds:

$$\vec{\Delta}_s = \sqrt{\vec{x}^2 + \vec{y}^2} - s^* \quad (10)$$

$$\vec{I}_s = \exp\left(-\frac{\vec{\Delta}_s^2}{2\sigma_s^2}\right) \quad (11)$$

In Eq. 11,  $\sigma_s = 0.5^\circ/\text{sec}$  represents the sensitivity to optic flow directions that deviate from the preferred speed. 192  
193

**MT unit activation** Each MT unit  $m$  integrates its input over time as a leaky integrator

$$\frac{dm}{dt} = -\alpha_{MT}m + (\beta_{MT} - m)I_{MT} \tag{12}$$

where  $\alpha_{MT} = 0.1$  represents the cell's passive decay rate and  $\beta_{MT} = 2.5$  represents the upper bound on each unit's activation. 194  
195

**Model area MSTd** 196

Parameter	Description	Value
$N_{MST}$	Number of MSTd units	169
$\gamma$	Controls center-peripheral bias in heading representation	0.5 (“peripheral model”), 2 (“central model”)
$\sigma_{MST}$	Controls size of MSTd RFs	77 pixels (50°)
$\alpha_{MST}$	MSTd activation passive decay rate	0.1
$\beta_{MST}$	MSTd activation upper bound	2.5

Table 3: Summary of default model MSTd parameters used in simulations.

**MSTd unit placement** To investigate how the placement of MSTd RFs influences heading estimates, we distributed  $N_{MST} = 169$  MSTd units randomly across 2D heading space with varying amounts of center-peripheral bias. We determined the position of each MSTd RF in polar coordinates  $(R, \Theta)$ , centered on the middle of the visual field  $\bar{c}$ . The angles  $(\Theta)$  spanned 0–360° in steps of  $1/N_{MST}$ , while each radius  $(R)$  was randomly sampled from a uniform distribution and transformed by a gamma function:

$$x_p \sim \mathcal{U} \left[ 0, \sqrt{c_x^2 + c_y^2} \right] \tag{13}$$

$$R = x_p^\gamma \tag{14}$$

The  $\gamma$  value controls the center-peripheral bias in the heading representation:  $\gamma < 1$  produces peripheral bias,  $\gamma > 1$  produces central bias, and  $\gamma = 1$  produces no bias. 197  
198

**MSTd net input** Each MSTd unit receives input from MT units tuned to directions that are locally compatible with the radial optic flow field that radiates from its preferred heading direction. For example, an MSTd unit tuned to a central heading would receive input from MT cells tuned to leftward motion on the left side of

the visual field and from those tuned to rightward motion on the right side of the visual field. We define the 2D position of the heading direction in the visual field as  $\vec{h}^*$ . The normalized vector that points in the appropriate radial direction for  $\vec{h}^*$  at the position of MT unit  $i$ 's RF ( $\vec{r}_i$ ) is:

$$\vec{u}_i = \frac{\vec{r}_i - \vec{h}^*}{\sqrt{(r_{x,i} - h_x)^2 + (r_{y,i} - h_y)^2}} \quad (15)$$

We subtract the preferred direction  $d_i^*$  of each MT unit  $i$  with the local direction  $\vec{u}_i$  that is appropriate for heading  $\vec{h}^*$  to determine their similarity. Non-exact matches between each pairs of vectors are weighted according to the cosine tuning function:

$$U_i = \max(2 \cos(\text{atan2}(u_{y,i}, u_{x,i}) - d_i^*)^q - 1, 0) \quad (16)$$

The power  $q \geq 1$  in Eq. 16 makes each MSTd unit less selective to non-exact matches, 199  
 which in our testing improved the overall accuracy of heading estimates compared to a 200  
 unit exponent. We set  $q = 2$  in the default model and note that the equation as 201  
 written redistributes the cosine values from the interval  $[-1, 1]$  to  $[0, 1]$  for even 202  
 powers. Multiplication by 2 and subtraction by 1 restores the original range. The 203  
 $\max(\cdot, 0)$  operation represents half-wave rectification, which sets values below 0 to 0. 204  
 Note that the cosine tuning is mathematically equivalent to a dot product between the 205  
 MT direction and MSTd radial pattern template vectors that is used in some template 206  
 models (Warren & Saunders, 1995; Perrone, 2012; Layton et al., 2012). 207

Each local pattern match signal  $U_i$  is weighted by the activation of MT unit ( $m_i$ ) at the same position and by the inverse distance between the MT RF center  $\vec{r}_i$  and the heading direction  $\vec{h}^*$ , both of which are common computations in template models (Warren & Saunders, 1995; Royden, 2002; Layton et al., 2012).

$$\tilde{I}_{MST,i} = U_i \frac{m_i}{\sqrt{2\pi\sigma_{MST}^2}} \exp\left(-\frac{(h_x - r_{x,i})^2 + (h_y - r_{y,i})^2}{2\sigma_{MST}^2}\right) \quad (17)$$

The parameter  $\sigma_{MST}$  controls the effective extent of the MSTd receptive field. In the 208  
 default model, we set  $\sigma_{MST} = 50^\circ$ , which corresponds roughly to a large  $100^\circ$  RF size 209  
 in agreement with *in vivo* MSTd cell properties (Tanaka et al., 1986). 210

The net input signal that each MSTd unit receives is computed by Eq. 17, averaged over the number of MT inputs:

$$I_{MST} = \frac{1}{N_{MT}} \sum_{j=1}^{N_{MT}} \tilde{I}_{MST,j} \quad (18)$$

**MSTd activation** Each MSTd unit  $M$  integrates its input over time as a leaky integrator

$$\frac{dM}{dt} = -\alpha_{MST}M + (\beta_{MST} - M) I_{MST} \quad (19)$$

where  $\alpha_{MST} = 0.1$  represents the cell's passive decay rate and  $\beta_{MST} = 2.5$  represents the upper bound on each unit's activation. 211  
212

## Simulation experiments 213

Experiment	Description	Parameter	Values
MSTd heading	Center-peripheral bias in heading representation	$\gamma$	[0.1, 0.2, 0.5, 1, 2, 5, 10]
MSTd RF size	Standard deviation of Gaussian RF	$\sigma_{MSTd}$	[11.3°, 21.8°, 38.7°, 50.2°, 58.0°, 63.4°] ( [12.8, 25.6, 51.2, 76.8, 102.4, 128 ] pixels)
MSTd direction	Degree of intolerance to MT inputs that mismatch the preferred radial pattern	$q$	[1, 2, 4, 6, 8]
MT direction	maximum extent of random deviation between the radial direction and each MT preferred direction	$\sigma_d$	[0°, 60°, 120°, 180°, 240°, 300°, 360°]
MT speed	Baseline beta distribution shape used to sample speed preferences of each MT unit	$k_s$	4
MT speed + RF	Intercept of linear regression fit that determines RF size from eccentricity	$\beta_{ecc,0}$	0.19° (0.42 pixels)
MT speed + RF	Slope of linear regression fit that determines RF size from eccentricity	$\beta_{ecc,1}$	[0.27, 0.54, 0.81, 1.07] ([0.3, 0.6, 0.9, 1.2] pixels)

Table 4: Parameters varied from default model in simulation experiments.

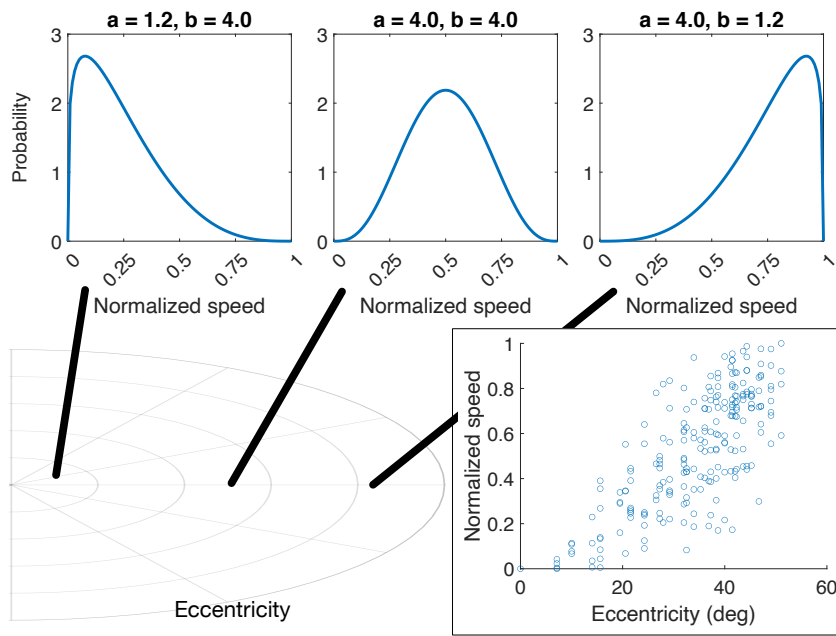


Figure 4: Methodology used to scale speed preference with eccentricity in MT speed tuning experiment. The eccentricity of a MT unit's RF (bottom left) is used to parameterize the beta distribution that is sampled to determine the preferred speed (top). For example, the preferred speed of a foveal MT unit is drawn from beta distribution with most of the density concentrated around slow speeds (top-left plot). The bottom-right scatter plot shows the preferred speeds in the simulated population normalized to range of the optic flow speeds present in the stimulus

We performed three main simulation experiments on model area MSTd involving 214  
the distribution of units along the central-peripheral axis, RF size, and direction 215  
selectivity. We performed two additional experiments on model area MT focusing on 216  
direction selectivity and speed selectivity. Table 4 enumerates specified parameter 217  
values used in each experiment. 218

**Experiment: MSTd central-peripheral heading tuning** 219

We varied the model parameter  $\gamma$  (Eq. 14) to affect the distribution of heading tuning 220  
along the center-peripheral axis:  $\gamma < 1$  produces peripheral bias,  $\gamma > 1$  produces 221  
central bias, and  $\gamma = 1$  produces no bias. 222

**Experiment: MSTd RF size** 223

We varied the  $\sigma_{MSTd}$  standard deviation parameter that controls the extent of the 224  
Gaussian MSTd RF (Eq. 17). 225

**Experiment: MSTd direction selectivity** 226

We varied the exponent parameter  $q$  in Eq. 16 that controls the sensitivity of each 227  
MSTd cell to MT inputs that deviate from the radial directions. 228

**Experiment: MT direction selectivity** 229

We varied the  $\sigma_d$  standard deviation parameter that controls the maximum random 230  
deviation of each MT preferred direction from a radial pattern consistent with a 231  
central heading (Eq. 3). 232

**Experiment: MT speed tuning** 233

We implemented several alternatives to the uniform random model of MT speed 234  
tuning. We considered a model that discards speed information and bases heading 235

estimates on direction alone. We implemented this model by omitting  $I_s$  from Eq. 6. 236

Additionally, we implemented a probabilistic model wherein MT cells are more likely to demonstrate faster speed tuning at greater eccentricities (Mikami et al., 1986; Maunsell & Van Essen, 1983a). We parameterized the range of MT speed sensitivity around the dynamic range of the optic flow input. Each cell's preferred speed  $s^*$  obeys

$$s^* = x_s(\max \vec{s} - \min \vec{s}) + \min \vec{s} \quad (20)$$

where  $\vec{s}$  represents the optical speeds of the 300 input motion vectors (Eq. 5). In Eq. 20,  $x_s$  represents a random variate between 0 and 1 sampled from the beta distribution:

$$x_s \sim \text{Beta}[a_s, b_s] \quad (21)$$

As the top panel of Figure 4 illustrates, the bell-shaped beta density is centered when 237  
the shape parameters  $a_s$  and  $b_s$  are equal. When  $b_s$  remains fixed and  $a_s < b_s$ , the 238  
mean shifts left of center and the density concentrates around smaller x values (i.e. 239  
normalized speeds). Conversely, the mean shifts right of center when  $a_s$  remains fixed 240  
and  $a_s > b_s$ . Notice how the beta distribution gracefully handles the boundary 241  
conditions as the density concentrates nearby the minimum and maximum normalized 242  
speed values. 243

We tailored the shape parameters  $a_s$  and  $b_s$  around the eccentricity of each MT neuron's RF: the beta density spanned a continuum between being concentrated around small normalized speeds for cells at small eccentricities and around large normalized speeds for cells at large eccentricities (Figure 4). To compute  $a_s$  and  $b_s$ , we calculated the eccentricity of each MT unit  $i$  as the normalized Euclidean distance  $E_{norm,i}$  relative to the center of the visual field:

$$E_{dist,i} = \sqrt{(r_{x,i} - c_x)^2 + (r_{y,i} - c_y)^2} \quad (22)$$

$$E_{norm,i} = \frac{E_{dist,i}}{\left(\sqrt{c_x^2 + c_y^2}\right)} \quad (23)$$

For MT cells with RFs that are positioned closer than halfway to the center of

visual field, we configured the shape parameters to place the mean of beta density on the left side of the support:

$$a_s = k_s \left( \frac{E_{norm}}{1 - E_{norm}} \right) \quad (24)$$

$$b_s = k_s \quad (25)$$

For MT cells with RFs that are positioned halfway or farther away from the center of visual field, we configured the shape parameters to place the mean of beta density on the right side of the support:

$$a_s = k_s \quad (26)$$

$$b_s = k_s \left( \frac{1}{E_{norm}} - 1 \right) \quad (27)$$

We fixed the baseline beta shape  $k_s = 4$  after simulations revealed that values 1–10 244  
did not impact the accuracy of model heading estimates. 245

Finally, we considered a speed tuning model that combines the eccentricity dependent speed scaling (Figure 4) with RF size scaling. We adapted the linear regression model that relates MT RF size and eccentricity scaling from Tanaka et al. (1986). The regression model has form:

$$y_{size} = \beta_{ecc,0} + \beta_{ecc,1}x_{ecc} \quad (28)$$

where  $x_{ecc}$  is the RF eccentricity in degrees,  $y_{size}$  is the square root of the MT RF 246  
area,  $\beta_{ecc,0}$  is the intercept, and  $\beta_{ecc,1}$  is the slope. We re-parameterized the fitted 247  
coefficients from the published values to  $\beta_{ecc,0} = 0.19^\circ$  and  $\beta_{ecc,1} = 0.27^\circ$  since our 248  
MT model RF ( $\sigma_r$ ; Eq. 7) is expressed with respect to RF radius rather than area. 249

## Simulation protocol 250

We computed the mean and variance of heading estimates over 50 runs of each 251  
simulation experiment. The optic flow stimuli remained the same across runs and 252  
variability in estimates reflects the random sampling of model tuning parameters on 253  
each run. We repeated this process 10 times for the noise stimuli, with optic flow 254

stimuli generated anew each time. 255

We used population vector decoding to estimate heading from the MSTd activation on each frame (Georgopoulos, Schwartz, & Kettner, 1986):

$$\tilde{h} = \frac{1}{\sum_{i=1}^{N_{MST}} M_j} \sum_{j=1}^{N_{MST}} h_{x,j}^* M_j \quad (29)$$

We focused on decoding the x coordinate of the heading direction given that the y coordinate remained constant across our stimuli. We computed a single horizontal heading estimate over each 60 frame video using an exponential moving average with parameter  $\lambda$ :

$$h_{est,t} = \lambda \tilde{h}_t + (1 - \lambda) h_{est,t-1} \quad (30)$$

where  $t$  represents the current time step. We set  $\lambda = 0.25$  to dampen instantaneous fluctuations in heading estimates using the recent history. 256  
257

### Software Accessibility 258

We implemented the model and performed simulations in MATLAB. The model code is available on GitHub. 259  
260

## Results 261

We organized our computational investigation into two parts. First, we focused on the impact of MSTd tuning on heading estimates (central-peripheral representation of heading, direction tuning, RF size). Second, we evaluated how MT tuning characteristics (direction tuning, speed tuning, and RF size) influenced heading signals in two qualitatively distinct MSTd models. 262  
263  
264  
265  
266

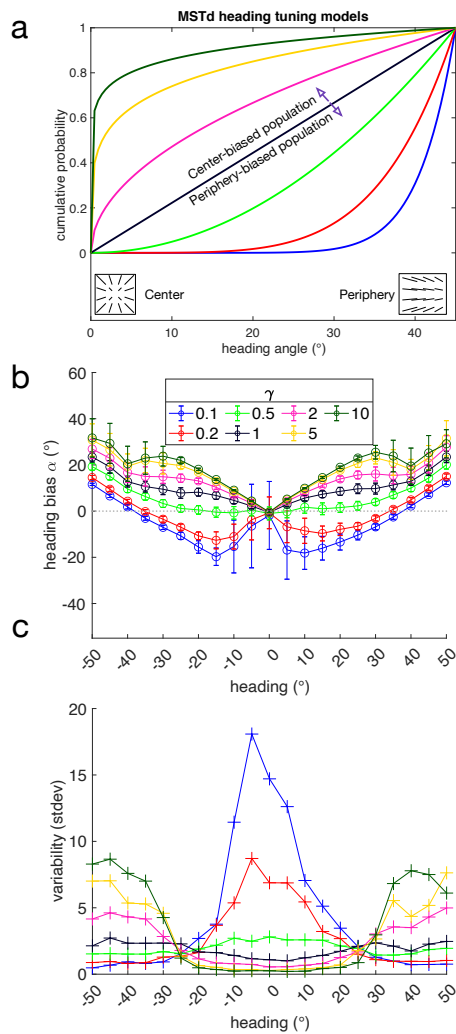


Figure 5: Simulations showing the effect of the heading representation of MSTd on estimates. (a) The cumulative probability of sampling each MSTd unit's preferred heading according to different MSTd models. The distribution of heading selectivity across the center-peripheral axis depends on each model's  $\gamma$  value. Only positive (rightward) headings are depicted, but the model samples headings from all 2D headings within the field of view. (b) Heading bias produced by simulating each model with self-motion along central-peripheral azimuthal axis within  $\pm 45^\circ$  of center. Negative (positive) biases correspond to heading errors toward the periphery (center). Negative (positive) heading values correspond to self-motion to the left (right) of the straight-ahead direction, respectively. Each point indicates the mean over 50 model runs and error bars show  $\pm 1$  standard deviation. (c) Variability (in standard deviations) obtained in the simulations plotted in (b).

## Effect of central-peripheral heading tuning in MSTd

We constructed 7 different models of MSTd to investigate how the representation of heading could impact the accuracy and precision of estimates. Each model is distinguished by its value of  $\gamma$ , the parameter that controls the extent to which the population heading preferences are biased along the central-peripheral axis (Figure 5a):  $\gamma < 1$  results in an overrepresentation of peripheral headings,  $\gamma > 1$  results in an overrepresentation of central headings, and  $\gamma = 1$  results in a uniform distribution of headings. Each MSTd model receives input from MT units, whose RFs are arranged in a regular grid instead of being randomly distributed. We made this decision to reduce internal model variability across simulations for factors unrelated to the main manipulation ( $\gamma$ ). However, simulations revealed the two methods of placing MT unit RFs did not differ in the average accuracy or the precision of the heading estimates (Figure 5-1).

Figure 5b shows the heading bias produced by each MSTd model for the 3D dot cloud optic flow stimuli. Heading bias is defined as the error in heading estimates, toward (positive) or away from (negative) the center (Figure 1d). As expected, models with an overrepresentation of central headings ( $\gamma > 1$ ) produced the lowest error when estimating central headings, while models with an overrepresentation of peripheral headings produced the lowest error when estimating peripheral headings ( $\gamma < 1$ ). It is noteworthy that all models, even those that overrepresent peripheral headings ( $\gamma < 1$ ), did not accurately estimate headings in the far periphery. This occurred because the FoE and surrounding motion may not appear within the 90° field of view. Motion nearby the FoE provides important information about heading (Crowell & Banks, 1996) and in its absence, MSTd heading detectors cannot estimate heading as accurately. The error is in the direction of the available motion vectors, resulting in an underestimation of heading (i.e. center bias).

Simulations reveal that a model with a weak-to-moderate overrepresentation of peripheral headings ( $\gamma = 0.5$ ) garnered the best overall accuracy (i.e. least absolute bias; mean absolute error (MAE) = 5.7°) across all of the conditions. This was the only model that garnered constant, nearly zero bias for central headings  $\leq \pm 20^\circ$ . The

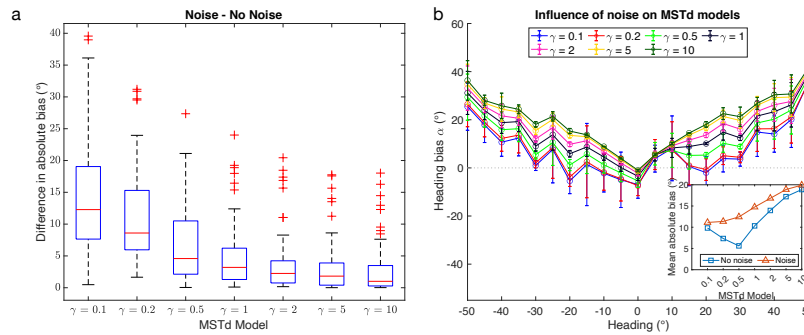


Figure 6: Simulations of optic flow containing noise using MSTd models with different heading representations. (a) Box plot showing the absolute difference between the No Noise condition and the noise stimuli that had 21 different headings and 3 noise levels (70%, 80%, or 90% noise dots). (b) Mean heading bias averaged across noise levels produced by each MSTd model for each heading (same plotting conventions as Figure 5). Inset compares mean absolute heading bias between the Noise (red) and No Noise (blue) stimuli, averaged across individual heading directions.

other MSTd models produced two qualitatively distinct patterns of bias. Models with 297  
a more extreme peripheral heading overrepresentation ( $\gamma < 0.5$ ) exhibited peripheral 298  
bias in their estimates of the central headings, approximately within  $\pm 35^\circ$ . Models 299  
with an overrepresentation of central headings ( $\gamma > 1$ ) demonstrated consistent center 300  
bias that grew with heading eccentricity. The model with uniform heading sensitivity 301  
( $\gamma = 1$ ) behaved similarly to those with an overrepresentation of central headings. 302

Figure 5c plots the variability in heading estimates obtained over the 50 runs of 303  
each model. For MSTd models with an overrepresentation of central headings, 304  
variability was small in the center and large in the periphery. The opposite was true 305  
for models that had an overrepresentation of peripheral headings: large variability for 306  
central heading and small variability for peripheral headings. Notably, the model that 307  
garnered the best overall accuracy ( $\gamma = 0.5$ ) garnered the lowest overall mean 308  
variability (1.7 stdevs). It also produced the most consistent variability across 309  
headings. Together, these results suggest that a MSTd model with the 310  
weak-to-moderate overrepresentation of peripheral headings yields the most accurate 311  
and precise heading estimates. 312

Next, we examined how the estimates produced by the different MSTd models were 313

influenced by optic flow that differs from the idealized patterns used to construct each 314  
MSTd unit's RF. We simulated each model using stimuli wherein we replaced 70–90% 315  
of the dots belonging to the 3D dot cloud with noise uncorrelated with the self-motion 316  
direction (Figure 2b). We henceforth refer to stimuli without noise as the “No Noise” 317  
condition. Figure 6a shows how the 63 heading estimates produced each MSTd model 318  
(21 headings x 3 noise levels) deviated from the No Noise condition. The median effect 319  
of noise in most cases was only several degrees despite the considerable differences in 320  
the heading representations across the models. While the central MSTd models 321  
( $\gamma > 1$ ) were only weakly affected by the noise, the baseline accuracy of these models 322  
is poor regardless of noise, especially compared to the peripheral models (compare 323  
Figure 5b and Figure 6b). For example, without noise the  $\gamma = 10$  model exhibits 324  
 $30^\circ$  heading error toward the center for  $\pm 50^\circ$  headings. 325

Noise did, however, influence MSTd models with an overrepresentation of 326  
peripheral headings ( $\gamma < 0.5$ ) to a greater extent, as indicated by the much higher 327  
medians and presence of more extreme absolute differences from the No Noise 328  
condition. The model with a weak-to-moderate overrepresentation of peripheral 329  
headings ( $\gamma = 0.5$ ) demonstrated the biggest mean shift in the accuracy of its 330  
estimates (Figure 6b inset). Recall that this model garnered the most accurate 331  
estimates in the No Noise condition. The greater influence of noise in the peripheral 332  
models increased the center bias (i.e. positive shift) for most headings (compare 333  
Figure 5b and Figure 6b). Despite the increased sensitivity to noise, peripheral MSTd 334  
models still produced the most accurate heading estimates (Figure 6b inset). 335

### Effect of MSTd RF size 336

MSTd neurons are well known to exhibit tremendous variation in their RF size, 337  
reaching  $100^\circ$  or more (Tanaka et al., 1986). We explored within the computational 338  
framework whether such large RF sizes are necessary to support accurate heading 339  
estimation. Given the qualitatively different patterns of heading bias produced by the 340  
center and peripheral MSTd models, we henceforth focus on two specific model 341  
instances: one with an overrepresentation of peripheral headings ( $\gamma = 0.5$ ; henceforth 342

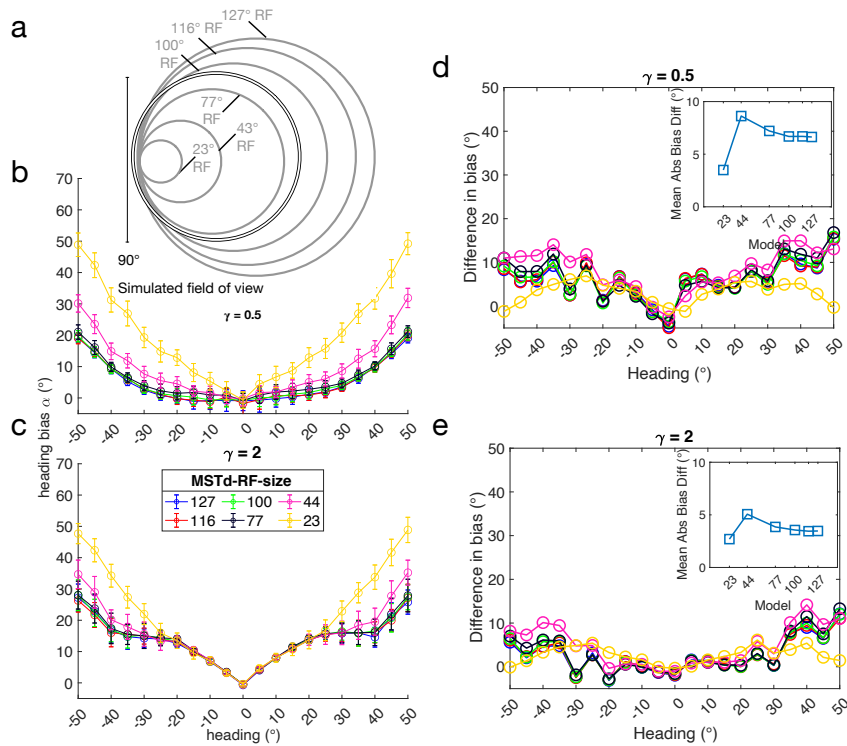


Figure 7: Simulations showing the effect of MSTd RF size on heading estimates. (a) Schematic showing the simulated MSTd RF sizes (gray circles) compared to the 90° simulated field of view (black circle). (b-c) Heading bias obtained over 50 runs of the peripheral (b;  $\gamma = 0.5$ ) and central (c;  $\gamma = 2$ ) MSTd models. (d-e) Difference in mean heading bias produced by the peripheral (d;  $\gamma = 0.5$ ) and central (e;  $\gamma = 2$ ) MSTd models between the Noise and No Noise conditions. Insets show the absolute difference in heading bias between the Noise and No Noise conditions averaged across headings. Positive values indicate increased bias toward the straight-ahead.

“peripheral model”) and one with an overrepresentation of central headings ( $\gamma = 2$ ; 343  
henceforth “central model”). 344

Figure 7a schematizes the simulated MSTd RF diameters (gray circles) that ranged 345  
from  $23^\circ$  to  $127^\circ$  relative to the  $90^\circ$  field of view (black circle). RFs larger than the 346  
field of view are worth considering because such units tuned to peripheral headings are 347  
capable of integrating motion at the far reaches of the opposite side of the visual field. 348  
Simulations of the peripheral model showed that RF size made little difference when 349  
estimating central headings (Figure 7b). The effect of RF size was different at the 350  
periphery: increasing MSTd RF size improved heading accuracy, but the improvement 351  
plateaued once the RF size reached  $77^\circ$ . The small  $23^\circ$  units produced more than 352  
twice the bias for peripheral headings than the larger units toward the center. This 353  
suggests that integrating contextual information over a larger area helps to mitigate 354  
the uncertainty in the periphery caused by the lack of a FoE within the field of view. 355  
Figure 7c shows the estimates produced by the central model. Once again, it produced 356  
less accurate heading estimates overall than the peripheral model. While the pattern 357  
of bias is similar, the increasing the RF size did not improve the estimates as much. 358

Figure 7d-e show the difference in bias between the Noise and No Noise conditions. 359  
On average, noise had a similar impact regardless of MSTd RF size. In all but the 360  
smallest RF size there was an increase in the heading bias toward the center at 361  
peripheral headings, but for most headings the effect was weak. The peripheral MSTd 362  
model exhibited the same qualitative effect, but demonstrated increased sensitivity 363  
compared to the central model. 364

### Effect of MSTd direction tuning 365

A key characteristic of template models of MSTd is that RFs are constructed from 366  
idealized patterns of radial optic flow (Figure 1a,c). Some template models make the 367  
strong assumption that each MSTd unit integrates only the set of MT directions that 368  
form the specific global pattern (Figure 8a; top) (Royden, 2002; Layton & Fajen, 369  
2016b), while others integrate at every visuotopic position a range of directional 370

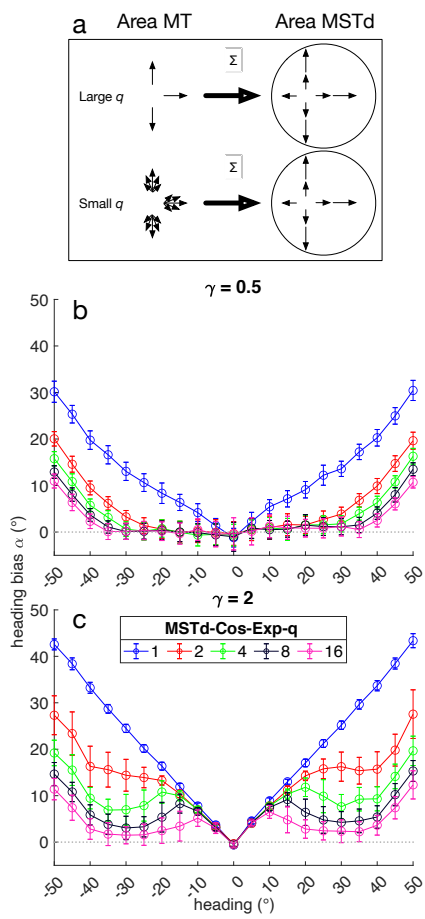


Figure 8: Simulations focusing on direction selectivity in MSTd. (a) We varied model parameter  $q$  that controlled the range of directions each MSTd unit integrated that deviated from the preferred radial pattern. Large  $q$  values increased the selectivity and in the extreme case, MSTd units would only integrate directions that exactly match the preferred radial pattern. Smaller  $q$  values increased the range of integrated directions, centered around each preferred radial direction. (b) Mean bias for each heading direction produced by the peripheral MSTd model configured with different  $q$  values. (c) Same as (b) except for the central MSTd model. Same plotting conventions as Figure 5.

inputs centered on the direction consistent with the radial pattern (Figure 8a; 371  
bottom) (Raudies & Neumann, 2010; Perrone, 1992). Before turning our focus to the 372  
impact of MT tuning on heading signals, we examined the extent to which the 373  
selectivity of each MSTd unit to directional inputs influences heading estimates. 374

We manipulated the selectivity of MSTd units directional inputs that deviate from 375  
each radial direction via the commonly used rectified cosine tuning function. This 376  
function weights the difference between the preferred radial direction and preferred 377  
directions of the MT units that send input (Eq. 16). The function ensures that the 378  
MSTd unit still responds maximally to the preferred heading because discrepant 379  
directions are down-weighted by the cosine function. To control the range of 380  
directional inputs that may activate the MSTd unit, we raised the cosine to the power 381  
 $q$  (Figure 8a). 382

Figure 8b shows the heading bias produced by the peripheral model. Increasing the 383  
directional selectivity substantially improved the accuracy across all non-zero headings. 384  
The most pronounced increase in accuracy occurred from  $q = 1$  and  $q = 2$  and higher 385  
exponents further improved the estimates in the periphery. The highest exponent 386  
values tests garnered accurate heading estimates for approximately the central  $70^\circ$  387  
heading directions. The central model yielded much less accurate heading estimates 388  
overall (Figure 8c). However, the effect of directional selectivity is similar to that in 389  
the peripheral model: larger powers reduced heading bias, albeit to a lesser extent. 390

In both models, simulations involving powers greater than 3 had the undesirable 391  
effect of making MSTd units so narrowly tuned to direction that occasionally some 392  
optic flow inputs would not activate any of the simulated MSTd units. This occurred 393  
because we simulated a limited number of MSTd units and there was no guarantee 394  
that MSTd contained a unit tuned to the exact heading in the optic flow input. In 395  
these situations, we re-ran the model with different random initial conditions until we 396  
obtained 50 valid heading estimates. Taken together, these simulations suggest that 397  
increased directional selectivity to the preferred pattern supports accurate self-motion 398  
estimation over a wider range of headings. However, extremely narrow direction 399  
tuning has the adverse effect of making neurons too selective for patterns, even for 400

those that deviate modestly from their preferred radial pattern of motion.

401

### Effect of MT direction tuning

402

Template models of MSTd predict that heading sensitivity largely emerges through the feedforward integration of MT signals. We explored how MT direction and speed tuning could influence heading estimate downstream in MSTd. We parameterized model MT direction tuning around the known population bias toward a global radial pattern (Albright, 1989). For example, MT units with RFs on the right side of the visual field are more likely to be tuned for rightward than leftward motion (Figure 9a; leftmost panel).

403

404

405

406

407

408

409

We tested how anchoring MT direction tuning to a radial pattern impacts model heading estimates. Figure 9a schematically depicts a continuum of constraints on the model direction tuning, ranging from strictly radial (left;  $\sigma_d = 0^\circ$ ) to uniform random (right;  $\sigma_d = 360^\circ$ ). Strongly enforcing the radial direction constraint ( $\sigma_d \approx 0^\circ$ ) resulted in substantial heading bias toward the center, giving rise to ‘V’-shaped bias curves in both peripheral (Figure 9b) and central (Figure 9c) MSTd models. Constraining the direction tuning within  $\pm 90^\circ$  of the radial direction ( $\sigma \leq 180^\circ$ ) improved the accuracy produced by both MSTd models in the periphery. Relaxing the tuning constraint beyond  $\pm 90^\circ$  did not further improve the accuracy. This coincides with the fact that the local direction of the optic flow cannot differ more than  $90^\circ$  in the optic flow stimuli that we used wherein heading varied along the horizon.

410

411

412

413

414

415

416

417

418

419

420

Estimates produced by the peripheral MSTd model were more greatly affected by noise than those produced by the center model (Figure 9d-e). In both models, the direction of the bias was toward the center. Taken together, this indicates that noise shifted MSTd activation toward neurons tuned to central headings to a greater extent than in the No Noise condition, despite the more limited resources dedicated toward representing central headings. The center bias grew in magnitude in both models when MT tuning deviated from the radial direction (Figure 9d-e insets). This occurred because random direction selectivity in MT is uncorrelated with radial

421

422

423

424

425

426

427

428

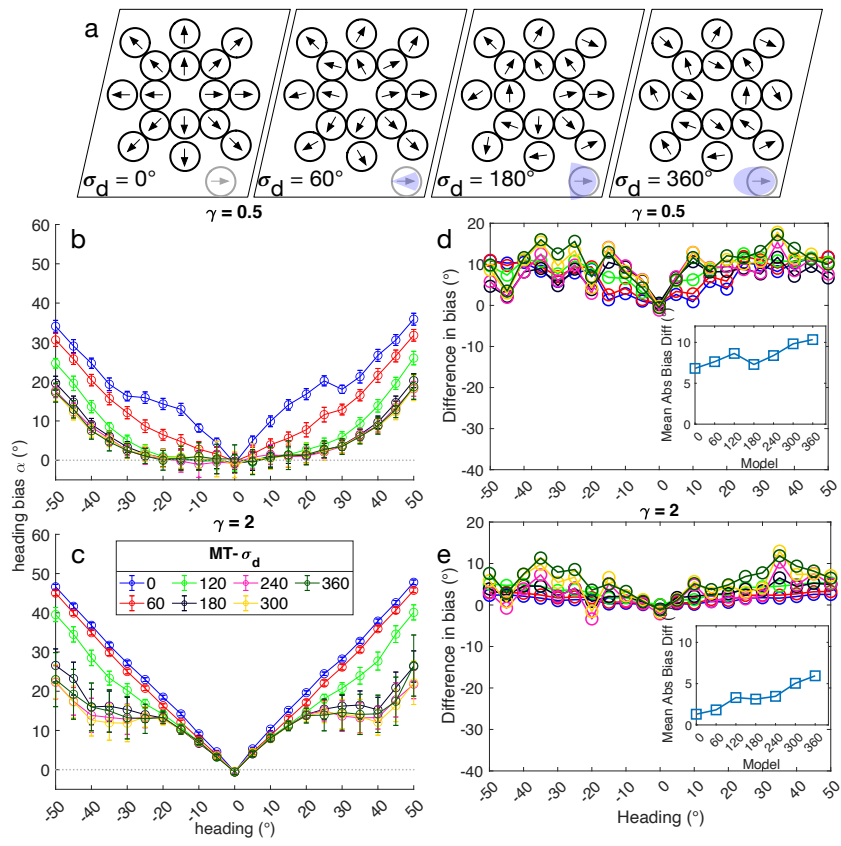


Figure 9: Simulations focusing on the effect of MT direction tuning on MSTd heading signals. (a) Schematic illustrating the influence of the parameter  $\sigma_d$  on MT direction selectivity. Values close to  $0^\circ$  result in direction tuning that resembles a radial pattern across the population. Larger values define the maximum bilateral extent to which MT units may deviate from the radial direction. The  $\sigma_d = 360^\circ$  condition created uniform random selectivity across MT. (b-c) Heading bias obtained over 50 runs from the peripheral (b;  $\gamma = 0.5$ ) and central (c;  $\gamma = 2$ ) MSTd models. Same plotting conventions as Figure 5. (d-e) Difference in mean heading bias produced by the peripheral (d;  $\gamma = 0.5$ ) and central (e;  $\gamma = 2$ ) MSTd models between the Noise and No Noise conditions. Same plotting conventions as Figure 7.

motion. Therefore, a greater proportion of the MT units signal noise in this case  
rather than the motion due to observer self-motion, which decreases sensitivity to the  
global pattern. It is noteworthy that the central MSTd model was only affected by  
noise when MT direction tuning was more randomly distributed (Figure 9e). This  
suggests that increased sensitivity to central headings compensates for the less  
selective direction signals in MT.

It is important to emphasize that despite its increased sensitivity to noise, the  
peripheral model still generally produces at least as accurate estimates as the central  
model. This is because the peripheral model demonstrates  $\approx 5^\circ$  more mean bias than  
the central model (compare Figure 9d-e insets), yet for many headings the baseline  
accuracy of the peripheral model is at least  $\approx 5^\circ$  more accurate, sometimes  
considerably more so (compare Figure 9b-c).

### Effect of MT speed tuning

We considered 4 different models of MT speed tuning (Figure 10a). In Model 1 we  
sampled MT speed preferences from a uniform random distribution. In Model 2 the  
probability that MT units were tuned to faster speeds increased with the eccentricity  
of their RFs (Maunsell & Van Essen, 1983b). Model 3 combines Model 2 with  
increasing RF size as a function of eccentricity (Raiguel et al., 1995; Tanaka et al.,  
1986). Finally, we considered a model wherein heading signals were determined on the  
basis of direction alone, ignoring speed (Model 0).

Figure 10b shows the heading estimates produced by the peripheral MSTd model  
combined with the four MT speed models. Only the direction-only (Model 0) and  
uniform random (Model 1) models accurately estimated heading for central headings.  
Model 2 with its increased likelihood of faster speed tuning at greater eccentricities  
produced peripheral bias for non-zero central headings. Also increasing the RF size  
with eccentricity (Model 3) amplified this bias. All four MT speed models  
demonstrated similar bias toward the center for peripheral headings. In the case of the  
center MSTd model (Figure 10c), none of the speed models appreciably impacted

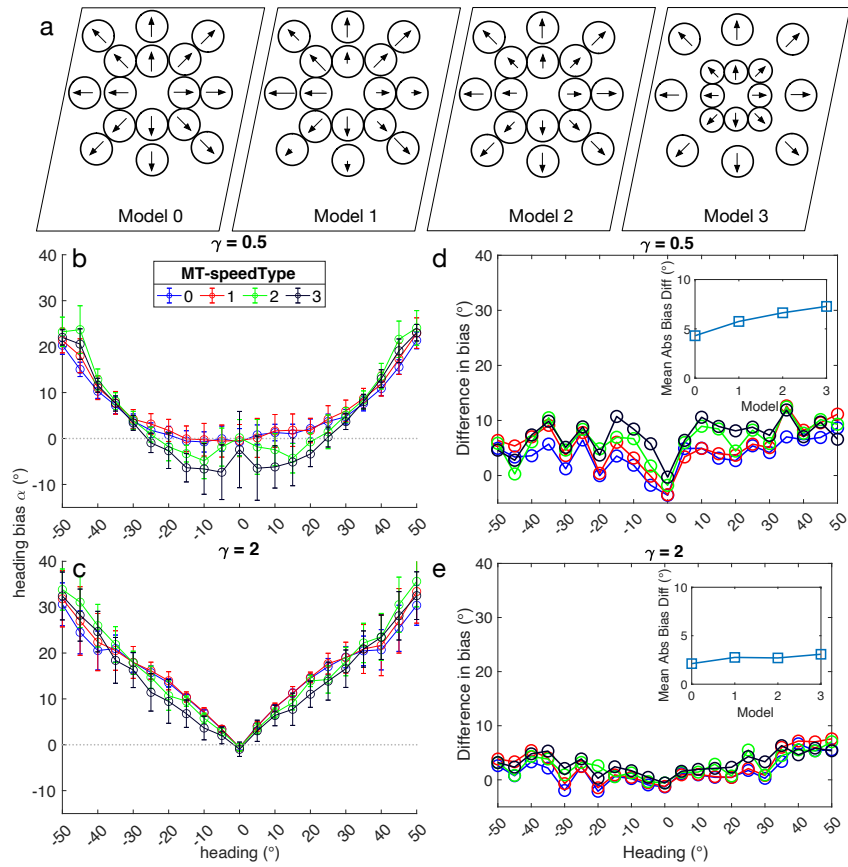


Figure 10: Simulations focusing on the effect of MT speed tuning on MSTd heading signals. (a) Schematic depiction of the four MT speed tuning models considered: (0) direction-only, (1) uniform random, (2) likelihood of faster preference increases with eccentricity, (3) likelihood of faster preference and RF size increase jointly with eccentricity. (b-c) Heading bias obtained over 50 runs from the peripheral (b;  $\gamma = 0.5$ ) and central (c;  $\gamma = 2$ ) MSTd models. Same plotting conventions as Figure 5. (d-e) Difference in mean heading bias produced by the peripheral (d;  $\gamma = 0.5$ ) and central (e;  $\gamma = 2$ ) MSTd models between the Noise and No Noise conditions. Same plotting conventions as Figure 7.

heading estimates. Finally, Figure 10d-e reveals that the center MSTd model was not  
substantially impacted by noise with any of the MT speed tuning models. The  
peripheral MSTd model exhibited increased sensitivity to noise, particularly in the  
models that scaled speed tuning with eccentricity (Models 2 and 3).

## Discussion

The present simulation study quantifies how physiological tuning characteristics in  
MT and MSTd influence heading signals within the template model computational  
framework. Physiological parameters in both areas exerted large, diverse effects on  
heading estimation. To encourage broad applicability of our results, we did not  
simulate any one specific model; rather, we simulated a combination of physiological  
constraints and core computations that broadly encapsulate mechanistic models of  
MT and MSTd.

### The impact of MSTd physiology on heading estimates

Our findings broadly support the notion that tuning properties in MSTd optimize the  
accuracy of heading estimation subject to neurophysiological constraints. In particular,  
we found that an overrepresentation of peripheral headings in model MSTd yielded  
the most accurate and precise heading estimates of the models tested. The model  
demonstrated sensitivity to noise, however, despite the noise, estimates remained more  
accurate than MSTd models with an overrepresentation of central headings.

Physiological studies have also reported peripheral bias in the heading tuning of  
MSTd neurons (Gu et al., 2006; Lappe, Bremmer, Pekel, Thiele, & Hoffmann, 1996).  
Such a model may perform well because the steepest portion of tuning curves across  
the population may capture a range of headings (Gu, Fetsch, Adeyemo, Deangelis, &  
Angelaki, 2010). We found that the peripheral bias in the heading representation also  
supported heading accuracy in the far periphery, despite the uncertainty created by  
the FoE falling near or outside the edge of the field of view. Note, however, that MSTd  
models with more extreme peripheral bias did not perform as well. Available neural

data appears to support a weak-to-moderate peripheral bias consistent with the best 484  
performing model: the largest number of MSTd neurons possess tuning to eccentric 485  
headings but not to those in the far periphery (Duffy & Wurtz, 1995; Gu et al., 2006). 486

### Large receptive fields and noise tolerance 487

The presence of MSTd neurons with large RF sizes spanning much of the visual field 488  
has long been noted (Tanaka et al., 1986; Duffy & Wurtz, 1991). Of the MSTd RF 489  
sizes that we tested,  $77^\circ$  and greater similarly supported the accuracy of heading 490  
estimates. The main advantage of such large RF units in our simulations was 491  
improved accuracy for peripheral heading estimates; units with RF sizes less than 492  
 $50^\circ$  did not demonstrate much difference when estimating central headings. 493  
Remarkably, 70-90% noise had a small average effect ( $5\text{--}10^\circ$  mean difference in bias), 494  
even in MSTd models with small RF units. This agrees with the accuracy of human 495  
heading perception under similarly low signal-to-noise ratio conditions (Van Den Berg, 496  
1992). It also supports what other computational studies have noted, that the 497  
computational mechanism by which MSTd neurons integrate motion signals according 498  
to radial templates can be robust under diverse conditions, even when the optic flow 499  
deviates from the preferred template patterns (Perrone, 1992; Layton & Fajen, 2016a; 500  
Royden, 2002; Browning et al., 2009). 501

### Human perception of peripheral headings 502

While the accuracy of humans heading judgments decreases with eccentricity, 503  
judgments plateau toward the periphery. This forms an approximately S-shaped (i.e. 504  
sigmoidal) curve (e.g. see Figure 1 of D'Avossa and Kersten (1996); Figure 2a of Sun 505  
et al. (2020)). Although this may seem at odds with the general pattern presented 506  
here whereby bias increases with eccentricity (e.g. Figure 5b), it is important to 507  
emphasize that we have plotted bias rather than actual estimates ("judgments"). 508  
Figure 11 depicts the results obtained from the MSTd heading tuning simulation 509  
experiment (Figure 5), both as heading bias (Figure 11a) and raw heading estimates 510

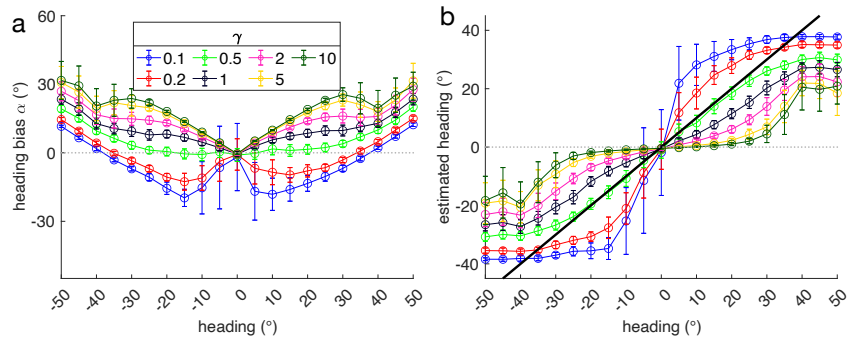


Figure 11: Simulation results from Figure 5b expressed with respect to bias (a) and raw heading estimates (b). Thick black curve in (b) indicates unity line. Same plotting conventions as Figure 5.

(Figure 11b). The S-shaped curve readily emerges for each MSTd model. Sun et al. 511  
 (2020) similarly show in their Figure 2a-b that human heading bias rises linearly and 512  
 raw judgments follow an S-shaped curve. 513

Toward the periphery, however, the amount of predicted bias diverges from 514  
 available human data, which generally show bias that does not exceed  $\approx 10^\circ$  (Cuturi 515  
 & Macneilage, 2013; Crane, 2012). Models with extreme overrepresentations of 516  
 peripheral headings ( $\gamma = 0.1$ ,  $\gamma = 0.2$ ) are the exception, though they produce zero 517  
 crossings in the bias to either side of the straight-ahead, which does not occur in 518  
 human judgments of forward headings. Figure 11b reveals that the large peripheral 519  
 bias corresponds to estimates within  $20\text{--}40^\circ$  of the straight-ahead. This substantial 520  
 center bias arises because the FoE is close to leaving the simulated  $90^\circ$  field of view 521  
 and the class of template models simulated here contains no mechanism to 522  
 “extrapolate” the FoE position. 523

We are unaware of any biologically-inspired models that have demonstrated 524  
 human-like heading predictions in the periphery. Computer vision algorithms that 525  
 triangulate the FoE position based on visible optic flow may yield improved heading 526  
 accuracy that more closely matches human performance in this scenario (Hildreth, 527  
 1992; Raudies & Neumann, 2013). However, another mechanism might be required 528

since triangulation ought to produce maximal bias when estimating lateral headings 529  
( $\pm 90^\circ$ ) and human bias reaches its maximum at  $\pm 45^\circ$  (Crane, 2012). One such 530  
mechanism may involve the subpopulation of MSTd neurons tuned to planar optic 531  
flow patterns (Duffy & Wurtz, 1995). Because motion vectors appear nearly parallel 532  
during self-motion along peripheral headings, planar cells may improve sensitivity to 533  
peripheral headings. Perception of peripheral headings and its underlying neural 534  
mechanisms warrant further investigation. 535

### Direction of human heading bias 536

Psychophysical studies have long observed that humans demonstrate center bias in 537  
their heading judgments (Llewellyn, 1971; Johnston et al., 1973; Cutting et al., 1992; 538  
Warren & Saunders, 1995; Royden & Hildreth, 1996; Layton & Fajen, 2016b; Sun et 539  
al., 2020). Sun et al. (2020) has examined this phenomenon and found that center bias 540  
reaches  $\approx 10^\circ$  for  $\pm 30^\circ$  headings. On the other hand, some studies of human heading 541  
perception have found the opposite pattern, bias toward the periphery (Crane, 2012; 542  
Cuturi & Macneilage, 2013). 543

Given how many times the bias has been reproduced under different experimental 544  
conditions, the discrepancy in direction across studies is unlikely to arise from specifics 545  
with the optic flow stimuli and viewing conditions. It is still possible, however, that 546  
the discrepancy could stem, at least in part, from methodological differences rather 547  
than a neural basis. One factor that distinguishes studies that have found peripheral 548  
bias is the use of orientation to indicate subjects' perceived heading. Subjects 549  
controlled the orientation of either a virtual arrow (Cuturi & Macneilage, 2013) or a 550  
physical dial (Crane, 2012) to match their perceived heading direction. Perhaps 551  
subjects systematically overestimate heading when making orientation-based 552  
judgments. Crane (2012) found evidence to support this possibility with his "Spoken" 553  
condition: stationary subjects sitting in darkness adjusted a physical dial to match a 554  
verbally spoken heading angle. The peripheral bias that emerged was qualitatively 555  
similar to that obtained in the visual (optic flow) condition, albeit weaker in 556  
magnitude. Including the full  $360^\circ$  range of headings in an experimental block of the 557

visual condition tripled the peripheral bias compared to limiting headings to  $\pm 45^\circ$  (Crane, 2012), further suggesting task-dependent effects. Cuturi and Macneilage (2013) reproduced the peripheral bias using a 2AFC staircase instead of the orientation-based paradigm, but only tested it for vestibular stimuli that subjects experienced while blindfolded. It is unclear whether optic flow would yield bias of the same direction. Indeed, Warren and Kurtz (1992) used a 2AFC procedure with optic flow stimuli and found center bias.

If the direction of bias has a neural basis, the physiological characteristics of MT and MSTd analyzed here may contribute. The MSTd model with a weak-to-moderate overrepresentation of peripheral headings ( $\gamma = 0.5$ ) (Figure 5b) captures the linear increase in center bias that reaches  $\approx 10^\circ$  at  $30^\circ$  eccentricity in Sun et al. (2020) (see their Figure 2b). However, it does not account for the variability in human heading judgments. Figure 5c shows that it demonstrates flat variability that decreases slightly with eccentricity, yet the average variability in human judgments grows with eccentricity (Sun et al., 2020; Crane, 2012; Cuturi & Macneilage, 2013). Interestingly, MSTd models that overrepresent central headings do demonstrate increased average variability in the periphery. In the case of the  $\gamma = 5$  and  $\gamma = 10$  models, the magnitude approximately matches that of human subjects (see Cuturi and Macneilage (2013) Figure 3e). Unfortunately, these models produce too much bias (Figure 5b) to plausibly account for the human data. If the  $\gamma = 0.5$  peripheral model that is most consistent with known physiology is actually most representative of MSTd, it is possible that the variability in human judgments arises from a source not modeled here.

MSTd models with greater sensitivity to peripheral headings ( $\gamma < 0.5$ ) reproduce the  $\approx 10^\circ$  peripheral bias (Crane, 2012; Cuturi & Macneilage, 2013), at least for central headings. As noted above, the simulated models qualitatively diverge from the human data in the periphery. Interestingly, the physiologically supported tendency for MT neurons to exhibit faster speed tuning and larger RFs with eccentricity yielded peripheral bias in the peripheral MSTd model ( $\gamma = 0.5$ ; Figure 10b), which otherwise only produced center bias (Figure 5b). This suggests that MT physiology supports peripheral heading bias when interacting with MSTd. Note that the shift from center

to peripheral bias emerged only for central headings and in the physiologically 589  
supported peripheral model of MSTd, not the central model ( $\gamma = 2$ ). Thus, MT 590  
tuning properties do not allow any of the MSTd models considered here to fully 591  
account for the peripheral bias produced by humans. 592

A pervasive assumption in our model construction and interpretation has been that 593  
tuning remains fixed, yet task demands and learning substantially influence dynamics 594  
in MT (Liu & Pack, 2017) and MSTd (Jacob & Duffy, 2015; Page & Duffy, 2018). It 595  
is possible that center and peripheral bias may arise in a single model in different 596  
contexts. For example, the visual system could dynamically increase the weight of MT 597  
neurons tuned to faster speeds if they signal valuable information that correlates with 598  
heading readouts, resulting in peripheral bias. Conversely, the weight of these MT 599  
neurons could be decreased if they do not meaningfully contribute to the readout, 600  
resulting in center bias. The brain might also favor readouts from subpopulations that 601  
less accurately encode heading to trade accuracy for rapid response time. Indeed, 602  
human heading perception depends on the temporal evolution of the optic flow 603  
field (Burlingham & Heeger, 2020; Layton & Fajen, 2016b). Future work should 604  
elucidate how dynamic and task-dependent factors influence heading perception. 605

## Acknowledgements 606

This work was supported by the Colby Academic Research Assistants / Presidential 607  
Scholar program (SY), Colby Summer Research Assistant Program (SY), and Office of 608  
Naval Research Grant ONR N00014-18-1-2283 (OWL). 609

## References 610

- Albright, T. (1989). Centrifugal directional bias in the middle temporal visual area 611  
(mt) of the macaque. *Vis Neurosci*, 2, 177–188. 612
- Born, R., & Bradley, D. (2005). Structure and function of visual area mt. *Annu Rev* 613  
*Neurosci*, 28, 157–189. 614

- Britten, K. (2008). Mechanisms of self-motion perception. *Annu Rev Neurosci*, *31*, 389–410. 615
- Britten, K., & Van Wezel, R. (1998). Electrical microstimulation of cortical area mst biases heading perception in monkeys. *Nature neuroscience*, *1*, 59. 616
- Browning, N., Grossberg, S., & Mingolla, E. (2009). Cortical dynamics of navigation and steering in natural scenes: Motion-based object segmentation, heading, and obstacle avoidance. *Neural Netw*, *22*(10), 1383–1398. 617
- Burlingham, C., & Heeger, D. (2020). Heading perception depends on time-varying evolution of optic flow. *Proc Natl Acad Sci U S A*, *117*(52), 33161–33169. 618
- Crane, B. (2012). Direction specific biases in human visual and vestibular heading perception. *PLoS One*, *7*(12), e51383. 619
- Crowell, J., & Banks, M. (1996). Ideal observer for heading judgments. *Vision research*, *36*(3), 471–490. 620
- Cutting, J., Springer, K., Braren, P., & Johnson, S. (1992). Wayfinding on foot from information in retinal, not optical, flow. *J Exp Psychol Gen*, *121*(1), 41–72. 621
- Cuturi, L., & Macneilage, P. (2013). Systematic biases in human heading estimation. *PLoS One*, *8*(2), e56862. 622
- Deangelis, G., & Uka, T. (2003). Coding of horizontal disparity and velocity by mt neurons in the alert macaque. *J Neurophysiol*, *89*(2), 1094–1111. 623
- Duffy, C., & Wurtz, R. (1991). Sensitivity of mst neurons to optic flow stimuli. i. a continuum of response selectivity to large-field stimuli. *Journal of neurophysiology*, *65*(6), 1329–1345. 624
- Duffy, C., & Wurtz, R. (1995). Response of monkey mst neurons to optic flow stimuli with shifted centers of motion. *Journal of Neuroscience*, *15*(7), 5192–5208. 625
- D'avossa, G., & Kersten, D. (1996). Evidence in human subjects for independent coding of azimuth and elevation for direction of heading from optic flow. *Vision research*, *36*(18), 2915–2924. 626
- Georgopoulos, A., Schwartz, A., & Kettner, R. (1986). Neuronal population coding of movement direction. *Science*, *233*(4771), 1416–1419. 627
- Gibson, J. J. (1950). *The perception of the visual world*. Houghton Mifflin. 628
- Graziano, M., Andersen, R., & Snowden, R. (1994). Tuning of mst neurons to spiral motions. *J Neurosci*, *14*(1), 54–67. 629

- Gu, Y., Deangelis, G., & Angelaki, D. (2012). Causal links between dorsal medial superior temporal area neurons and multisensory heading perception. *Journal of Neuroscience*, *32*(7), 2299–2313.
- Gu, Y., Fetsch, C., Adeyemo, B., Deangelis, G., & Angelaki, D. (2010). Decoding of mstd population activity accounts for variations in the precision of heading perception. *Neuron*, *66*(4), 596–609.
- Gu, Y., Watkins, P., Angelaki, D., & Deangelis, G. (2006). Visual and nonvisual contributions to three-dimensional heading selectivity in the medial superior temporal area. *J Neurosci*, *26*(1), 73–85.
- Hatsopoulos, N., & Jr, W. (1991). Visual navigation with a neural network. *Neural Networks*.
- Hildreth, E. (1992). Recovering heading for visually-guided navigation. *Vision research*, *32*(6), 1177–1192.
- Jacob, M., & Duffy, C. (2015). Steering transforms the cortical representation of self-movement from direction to destination. *J Neurosci*, *35*(49), 16055–16063.
- Johnston, I., White, G., & Cumming, R. (1973). The role of optical expansion patterns in locomotor control. *Am J Psychol*, *86*(2), 311–324.
- Lappe, M., Bremmer, F., Pikel, M., Thiele, A., & Hoffmann, K. (1996). Optic flow processing in monkey sts: a theoretical and experimental approach. *J Neurosci*, *16*(19), 6265–6285.
- Layton, O., & Fajen, B. (2016a). Competitive dynamics in mstd: A mechanism for robust heading perception based on optic flow. *PLoS computational biology*, *12*(6), e1004942.
- Layton, O., & Fajen, B. (2016b). The temporal dynamics of heading perception in the presence of moving objects. *J Neurophysiol*, *115*(1), 286–300.
- Layton, O., Mingolla, E., & Browning, N. (2012). A motion pooling model of visually guided navigation explains human behavior in the presence of independently moving objects. *Journal of vision*, *12*(1), 20–20.
- Liu, L., & Pack, C. (2017). The contribution of area mt to visual motion perception depends on training. *Neuron*, *95*(2), 436–446.e3.
- Llewellyn, K. (1971). Visual guidance of locomotion. *J Exp Psychol*, *91*(2), 245–261.
- Longuet-Higgins, H., & Prazdny, K. (1980). The interpretation of a moving retinal

- image. *Proc. R. Soc. Lond. B*, 208(1173), 385–397. 679
- Maunsell, J., & Van Essen, D. (1983a). The connections of the middle temporal visual 680  
area (mt) and their relationship to a cortical hierarchy in the macaque monkey. 681  
*Journal of Neuroscience*, 3(12), 2563–2586. 682
- Maunsell, J., & Van Essen, D. (1983b). Functional properties of neurons in middle 683  
temporal visual area of the macaque monkey. ii. binocular interactions and 684  
sensitivity to binocular disparity. *J Neurophysiol*, 49(5), 1148–1167. 685
- Mikami, A., Newsome, W., & Wurtz, R. (1986). Motion selectivity in macaque visual 686  
cortex. ii. spatiotemporal range of directional interactions in mt and v1. *J* 687  
*Neurophysiol*, 55(6), 1328–1339. 688
- Mineault, P., Khawaja, F., Butts, D., & Pack, C. (2012). Hierarchical processing of 689  
complex motion along the primate dorsal visual pathway. *Proc Natl Acad Sci U* 690  
*S A*, 109(16), E972–80. 691
- Page, W., & Duffy, C. (2018). Path perturbation detection tasks reduce mstd 692  
neuronal self-movement heading responses. *J Neurophysiol*, 119(1), 124–133. 693
- Perrone, J. (1992). Model for the computation of self-motion in biological systems. 694  
*JOSA A*, 9(2), 177–194. 695
- Perrone, J. (2012). A neural-based code for computing image velocity from small sets 696  
of middle temporal (mt/v5) neuron inputs. *J Vis*, 12(8). 697
- Perrone, J., & Stone, L. (1998). Emulating the visual receptive-field properties of mst 698  
neurons with a template model of heading estimation. *Journal of Neuroscience*, 699  
18(15), 5958–5975. 700
- Raiguel, S., Van Hulle, M., Xiao, D., Marcar, V., & Orban, G. (1995). Shape and 701  
spatial distribution of receptive fields and antagonistic motion surrounds in the 702  
middle temporal area (v5) of the macaque. *Eur J Neurosci*, 7(10), 2064–2082. 703
- Raudies, F., & Neumann, H. (2010). A model of neural mechanisms in monocular 704  
transparent motion perception. *J Physiol Paris*, 104(1-2), 71–83. 705
- Raudies, F., & Neumann, H. (2013). Modeling heading and path perception from optic 706  
flow in the case of independently moving objects. *Front Behav Neurosci*, 7, 23. 707
- Royden, C. (2002). Computing heading in the presence of moving objects: a model 708  
that uses motion-opponent operators. *Vision research*, 42(28), 3043–3058. 709
- Royden, C., & Hildreth, E. (1996). Human heading judgments in the presence of 710

- moving objects. *Percept Psychophys*, 58(6), 836–856. 711
- Sun, Q., Zhang, H., Alais, D., & Li, L. (2020). Serial dependence and center bias in 712  
heading perception from optic flow. *J Vis*, 20(10), 1. 713
- Tanaka, K., Hikosaka, K., Saito, H.-A., Yukie, M., Fukada, Y., & Iwai, E. (1986). 714  
Analysis of local and wide-field movements in the superior temporal visual areas 715  
of the macaque monkey. *Journal of Neuroscience*, 6(1), 134–144. 716
- Van Den Berg, A. (1992). Robustness of perception of heading from optic flow. *Vision 717  
research*, 32(7), 1285–1296. 718
- Van Essen, D., & Maunsell, J. (1983). Hierarchical organization and functional 719  
streams in the visual cortex. *Trends in neurosciences*, 6, 370–375. 720
- Warren, W., & Hannon, D. (1988). Direction of self-motion is perceived from optical 721  
flow. *Nature*, 336(6195), 162–163. 722
- Warren, W., & Kurtz, K. (1992). The role of central and peripheral vision in 723  
perceiving the direction of self-motion. *Percept Psychophys*, 51(5), 443–454. 724
- Warren, W., & Saunders, J. (1995). Perceiving heading in the presence of moving 725  
objects. *Perception*, 24(3), 315–331. 726

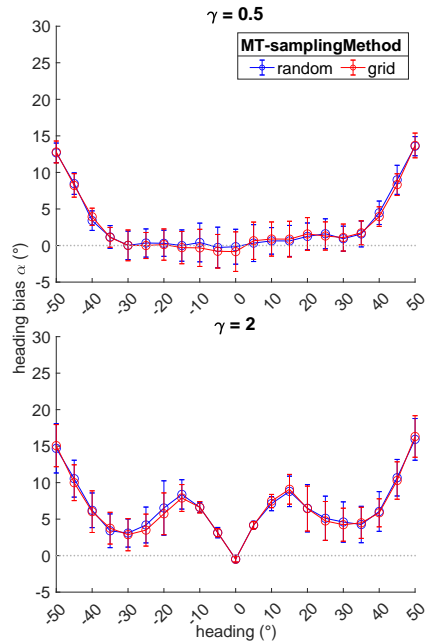


Figure 1: Heading bias produced by MSTd tuning models with an overrepresentation of central (a;  $\gamma = 2$ ), and peripheral (b;  $\gamma = 0.5$ ). The (“grid”) condition reflects simulations shown in Figure 5 in which MT cells were arranged in a two-dimensional rectangular grid. The random condition placed MT units in random visuotopic positions.

## Extended Data

### Effect of MT cell placement

Our goal for the simulations depicted in Figure 5 was to focus on the influence of MSTd tuning on heading estimation while maintaining a consistent model MT. Toward this end, we distributed MT units in a two-dimensional rectilinear grid; positioning MT RFs randomly, as we do in MSTd, might contribute error and variability to heading estimates unrelated to MSTd. Given that an even distribution of MT RFs across visuotopic space may not be a plausible assumption, we repeated the simulations whose results are shown in Figure 5 wherein MT RFs were placed randomly for two of the MSTd tuning models. As Figure 5-1 shows, there is no meaningful difference in mean heading errors and variability when placing placing MT units randomly and on a regular 2D grid.